Journal of
Materials Chemistry A

Materials for energy and sustainability

Accepted Manuscript

This article can be cited before page numbers have been issued, to do this please use: S. Eslava, M. Yang, H. Ye, Z. Meng, A. Pedersen, J. Parker, S. J. Haigh, H. Luo, H. H. H. Kristoffersen, J. Rossmeisl, M. M. Titirici, A. Hankin and J. Barrio, *J. Mater. Chem. A*, 2026, DOI: 10.1039/D6TA02778D.

ROYAL SOCIETY OF CHEMISTRY

rsc.li/materials-a

View Article Online
DOI: 10.1039/D6TA02778D

Ni–NC and Fe–NC Single-Atom Catalysts on Ti-doped Hematite for Selective Photoelectrochemical Glycerol Oxidation

Mengya Yang[a], Hanzhi Ye[a], Zhe Meng[b], Angus Pedersen[a], Joseph Parker[c], Sarah J. Haigh[c], Hui Luo[d], Henrik H. Kristoffersen[b], Jan Rossmeisl[b], Magda Magdalena Titirici[a,e], Anna Hankin[a], Jesús Barrio[a], Salvador Eslava* [a*]

[a] Department of Chemical Engineering and Centre for Processable Electronics, Imperial College London, SW7 2AZ, London, United Kingdom

[b] Department of Chemistry, University of Copenhagen, Copenhagen 2100, Denmark

[c] Department of Materials and National Graphene Institute, University of Manchester, M13 9PL, United Kingdom

[d] School of Engineering, University of Surrey, Guildford, GU2 7XH, United Kingdom

[e] Advanced Institute for Materials Research (WPI-AIMR), Tohoku University, 2-1-1 Katahira, Aoba-ku, Sendai, Miyagi, 980-8577, Japan

*E-mail: j.barrio-hermida@imperial.ac.uk; s.eslava@imperial.ac.uk

Abstract

Glycerol, a major byproduct of biodiesel production, can be selectively oxidized into high-value chemicals; however, efficient and selective conversion remains challenging due to complex C–O bond cleavage pathways. Photoelectrochemical glycerol oxidation with α-Fe_2O_3 photoanodes could offer a sustainable solution, but α-Fe_2O_3 suffers from inadequate charge separation and surface catalytic activity. Herein, we address these challenges by constructing hybrid photoanodes through integration of Ti-doped α-Fe_2O_3 (Ti–Fe_2O_3) with single metal atom catalysts in N-containing carbon (M–NC, M = Fe or Ni). The structural and functional synergy of Ti–Fe_2O_3/M–NC photoanodes was investigated using physicochemical characterization, photoelectrochemical measurements, and density functional theory (DFT) calculations. Formation of a Schottky junction at the Ti–Fe_2O_3/M–NC interface generates a built-in electric field that enhances charge-carrier separation and directional hole transfer to M–NC active sites. Consequently, Ti–Fe_2O_3/Ni–NC and Ti–Fe_2O_3/Fe–NC achieve photocurrent densities of 2.2 and 1.9 mA cm^{-2} at +1.23 V_{RHE}, representing ~3- and ~2.4-fold improvements over bare Ti–Fe_2O_3 (0.8 mA cm^{-2}). Moreover, M–NC incorporation enables tuning of the product selectivity: Ni–NC favors glyceric acid formation (~80% selectivity), whereas Fe–NC promotes glycolic acid production (~74% selectivity) at +0.8 V_{RHE}. With increasing applied potential (from +0.8 to +1.2 V_{RHE}), Ni–NC

View Article Online
DOI: 10.1039/D6TA02778D

induces pronounced changes in product distribution to formic acid, while Fe–NC maintains high glycolic acid selectivity with enhanced yields. DFT calculations attribute these metal-dependent selectivity trends to intrinsic differences in oxidation activity between Fe–NC and Ni–NC. Selectivity changes of Ni–NC may also arise from oxidized Ni clusters formation, as confirmed by post-reaction microscopy. This work highlights the potential of Ti–Fe_2O_3/M–NC photoanodes for selective biomass valorization and solar-driven photoelectrochemical reactions.

Keywords: Single-atom catalysts; hematite photoanodes; photoelectrochemical glycerol oxidation; product selectivity; density functional theory; renewable energy conversion

1 Introduction

As a major byproduct of biodiesel production, glycerol ($C_3H_8O_3$) can be selectively oxidized into value-added chemicals such as dihydroxyacetone (DHA), lactic acid (LA), glyceric acid (GLA), glycolic acid (GA), and formic acid (FA).[1, 2] The glycerol oxidation reaction (GOR) involves complex cleavage of C–O bonds at different molecular positions, necessitating the development of highly selective catalysts with well-defined active sites to enhance reaction kinetics and product selectivity.[3] Photoelectrochemical glycerol oxidation (PEC GOR) using n-type transition metal-based photoanodes such as hematite (α-Fe_2O_3),[4] bismuth vanadate ($BiVO_4$),[5] graphitic carbon nitride (g-C_3N_4),[6] or different metal oxides represents a sustainable approach for glycerol valorization under mild conditions.[7, 8] These photoanodes are attractive due to their abundance, affordability, and favorable interactions with carbon-containing species, enabling environmentally benign production of solar-driven chemicals.[9, 10] Among various n-type transition metal-based electrodes, hematite has been widely studied as a photoanode material owing to its suitable bandgap (~2.0 eV) for solar absorption, excellent chemical stability, and low cost.[11] However, α-Fe_2O_3 suffers from intrinsic limitations, including low charge-carrier mobility (~10^{-2} cm^2 V^{-1} s^{-1}), poor electrical conductivity (10^{-14} Ω^{-1} cm^{-1}), short minority carrier diffusion lengths (2–4 nm), and poor surface catalytic activity, which collectively hinder charge transport, separation, and interfacial reaction kinetics.[7, 8] To mitigate these challenges, the integration of co-catalysts with α-Fe_2O_3 to construct a composite catalytic system has emerged as a promising approach.

Among different co-catalysts, earth-abundant transition-metal-based catalysts have emerged as promising candidates for GOR, with Ni-based catalysts being particularly attractive due to their relatively low overpotentials.[12, 13] In addition, single-atom catalysts have gained considerable attention

View Article Online
DOI: 10.1039/D6TA02778D

due to their unique and tunable electronic structures, maximized atomic utilization, and uniform active centers.[14, 15] Anchoring precious metal single atoms directly on metal oxide photoelectrodes can enhance surface reaction kinetics. For instance, Feng et al. designed Pt single site catalysts on the surface of WO_3, showing current densities of up to 2.85 mA cm^{-2} and 60% Faradaic efficiency toward dihydroxyacetone production.[16] However, directly anchoring precious metal single sites onto the oxide surface of photoanodes present several challenges: 1) limited control over the coordination environment, which strongly influences band structure and reactivity,[17] 2) leaching of precious metals in commonly used alkaline electrolytes,[18] and 3) variable behavior of such sites, which may act as active catalysts or as spectators.[19]

In this context, transition-metal single atoms anchored on N-doped carbon (M–NC), such as Ni–NC and Fe–NC, have emerged as a promising alternative. Their synthesis typically requires high-temperature pyrolysis (800-1000 ºC) to achieve sufficient electrical conductivity for electrochemical reactions. However, such conditions lead to undesirable side reactions during pyrolysis, such as carbothermal reduction of metal species at temperatures above 600 ^{o}C.[20, 21] This limitation has been addressed through decoupled synthesis strategies employing inactive metal templates (e.g., Mg or Zn) that facilitate MN_x site formation without undergoing carbothermal reduction.[22, 23] Subsequently, active metals such as Ni or Fe can be introduced at lower temperatures without affecting the bulk chemical or morphological properties of the NC support, enabling systematic structure-activity investigations of different single metal atoms on equivalent supports.[24-26] Owing to their excellent redox activity and tunable *d*-orbital electronic configurations, M–NC catalysts have demonstrated notable performance in various electrocatalytic reactions, including O_2, NO_3^- and CO_2 reduction.[25-27] Additionally, M–NC materials have been explored as bifunctional O_2 evolution and reduction systems;[28] however, the stability of their active sites under strongly oxidizing and reducing conditions remain a concern. For instance, Wan et al. reported the transformation of M–NC (M = Co, Ni or Fe) into amorphous (oxy)hydroxide clusters under O_2 evolution reaction conditions.[29] Furthermore, the NC support itself may undergo denitrogenation and carbon corrosion,[30-33] depending on its degree of graphitization. In contrast, GOR exhibits a significantly lower thermodynamic equilibrium potential than the O_2 evolution reaction (e.g. +0.091 V_{RHE} for glycerol oxidation to GLA versus +1.23 V_{RHE} for O_2 evolution),[10] suggesting that M–NC catalysts could operate more stably in the less oxidative GOR environment. Nevertheless, the role of M–NC catalysts in PEC GOR systems remains largely unexplored, particularly with respect to their influence on photogenerated charge-carrier dynamics, reaction pathways, product selectivity, and operational stability.

Herein, we report the development of hybrid photoanodes composed of Ti-doped α-Fe_2O_3 (Ti-Fe_2O_3) integrated with single-atom M–NC catalysts (Fe–NC or Ni–NC) for enhanced PEC GOR. By combining physicochemical characterization, photoelectrochemical analysis, and density functional theory (DFT)

View Article Online
DOI: 10.1039/D6TA02778D

calculations, we elucidate the role of M–NC catalysts in modulating surface reaction kinetics, improving photogenerated charge separation, and regulating product selectivity. The formation of a Schottky junction at the Ti-Fe_2O_3/M–NC interface facilitates charge-carrier separation and hole transfer to atomically dispersed active sites, resulting in markedly improved PEC performance. Moreover, Ti-Fe_2O_3/Ni–NC and Ti-Fe_2O_3/Fe–NC delivered photocurrent densities of 2.2 and 1.9 mA cm^{-2} at +1.23 V_{RHE}, representing ~3- and ~2.4-fold enhancements over bare Ti-Fe_2O_3, respectively. M–NC incorporation also tuned product selectivity, with Ni–NC favoring glyceric acid (~80%) and Fe–NC favoring glycolic acid (~74 %) at +0.8 V_{RHE}. At higher potentials, Ni–NC shifted selectivity toward formic acid, whereas Fe–NC retained high glycolic acid selectivity with improved yields. The distinct selectivity trends of Ni–NC and Fe–NC toward different glycerol oxidation products, highlighting the tunability of reaction pathways through the doped metal. This work demonstrates a promising strategy for integrating single-atom M–NC catalysts with hematite-based photoanodes, advancing the development of efficient and selective solar-driven biomass valorization systems.

2 Results and Discussion

The preparation of Ti–Fe_2O_3/M–NC (M = Ni or Fe) photoanodes is schematically illustrated in **Figure 1a** and described in detail in the Experimental Section (Supporting Information, SI). Briefly, Ti–Fe_2O_3 photoanodes were obtained by annealing hydrothermally grown Ti-doped β-FeOOH films in air up to 800 ºC. Ti doping was employed to enhance electrical conductivity, reduce recombination, and improve charge separation in hematite, thereby increasing the photocurrent.[34] 5% Ti doping level was selected based on our previous work.[35] Subsequently, the surface was modified with Ni–NC or Fe–NC single-atom catalysts prepared via a decoupled cation exchange protocol employing 2,4,6-triaminopyrimidine as an organic building block and $MgCl_2 \cdot 6H_2O$ as active site template and porogen.[25, 36] The crystalline structures of the prepared samples were examined by X-ray diffraction (XRD). As shown in **Figure 1b**, Ti–Fe_2O_3 exhibited characteristic diffraction peaks at 24.1, 33.2, 35.6, 49.5, and 54.3°, corresponding to the hematite (α) Fe_2O_3 phase (JCPDS No. 33-0664). Additional reflections at 26.6, 37.9, 51.8, 61.9, and 65.9° arose from the fluorine-doped tin oxide (FTO, JCPDS No. 41-1445) coated on the glass substrate. No additional diffraction peaks were observed after Ni–NC or Fe–NC loading, indicating the absence of detectable crystalline Ni- or Fe-containing phases. This is consistent with atomically dispersed metal sites embedded within a predominantly amorphous (partially graphitized) NC matrix or with loadings below the XRD detection limit. The morphology of the photoanodes was further investigated by field-emission scanning electron microscopy (FE-SEM). As shown in **Figures 1c–e** and **Figure S1**, Ti–Fe_2O_3 formed a highly porous nanostructure uniformly covering the FTO substrate, consisting of micrometer-scale agglomerates composed of ~100 nm nanoparticles. After deposition of M–NC catalysts, the porous Ti–Fe_2O_3 framework remained largely exposed, while additional thin

View Article Online
DOI: 10.1039/D6TA02778D

nanosheet-like features indicated with orange arrows attributed to the Ni–NC or Fe–NC species were observed (**Figure S1**), showing that M-NC is uniformly loaded on the Ti-Fe_2O_3 porous layer and confirming the successful incorporation of the catalysts on the photoanode absorption layer.

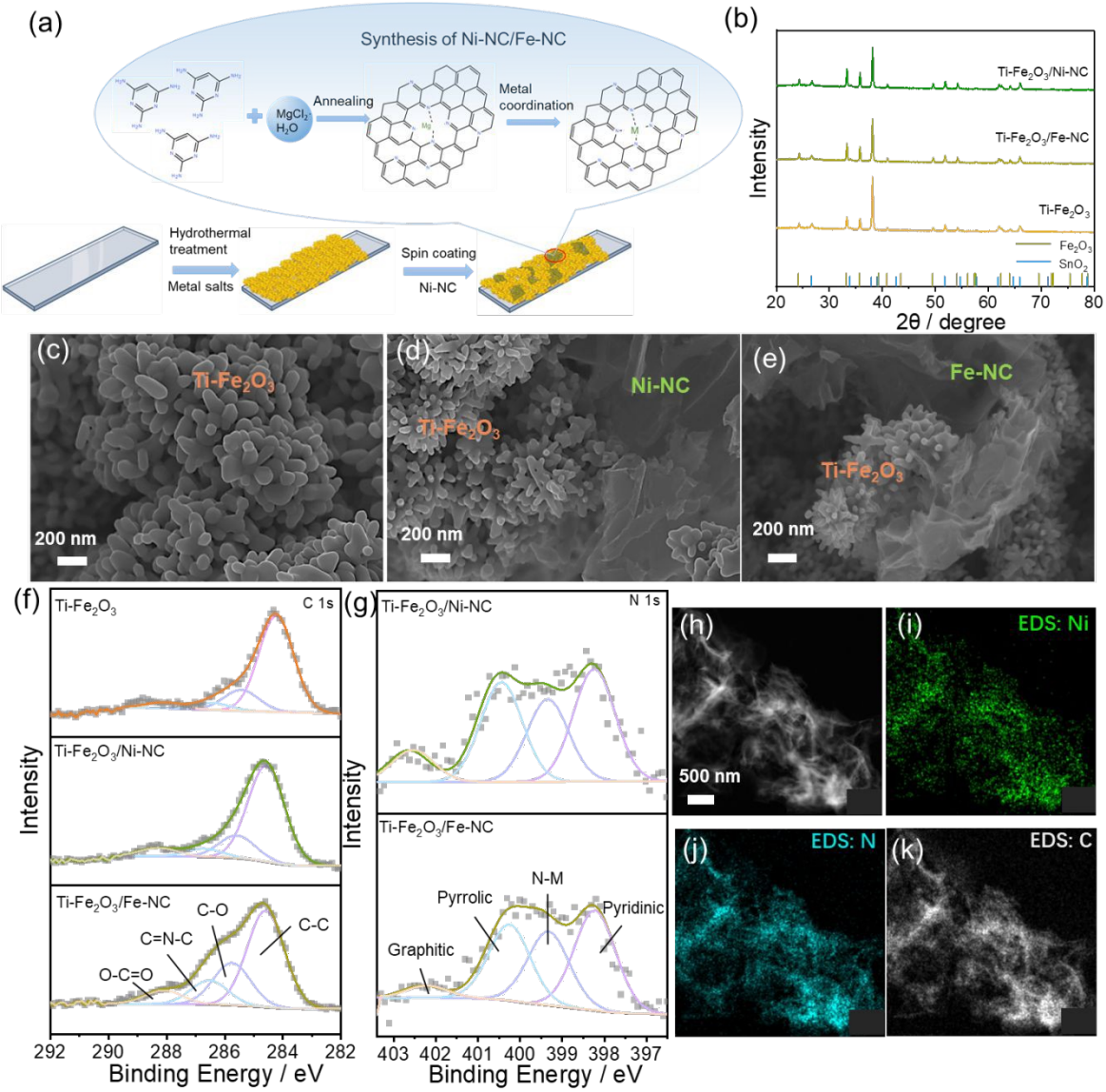

Figure 1. (a) Schematic illustration of the synthesis procedure for Ti–Fe_2O_3/M–NC (M = Ni or Fe) photoanodes. (b) XRD patterns of Ti–Fe_2O_3, Ti–Fe_2O_3/Ni–NC, and Ti–Fe_2O_3/Fe–NC. (c–e) FE-SEM, acquired using the in-column secondary electron (InLens) detector, of Ti–Fe_2O_3, Ti–Fe_2O_3/Ni–NC, and Ti–Fe_2O_3/Fe–NC. (f) High-resolution C 1s XPS spectra of Ti–Fe_2O_3, Ti–Fe_2O_3/Ni–NC, and Ti–Fe_2O_3/Fe–NC. (g) High-resolution N 1s XPS spectra of Ti–Fe_2O_3/Ni–NC and Ti–Fe_2O_3/Fe–NC. (h–k) HAADF-STEM micrographs and corresponding STEM–EDS elemental mappings of Ni–NC. Scale bars are identical for Figure h–k.

View Article Online
DOI: 10.1039/D6TA02778D

X-ray photoelectron spectroscopy (XPS) was employed to investigate the surface chemical composition and electronic states of the Ti–Fe_2O_3/M–NC hybrid photoanodes. The survey spectra (**Figure S2a**) confirmed the presence of Ti, Fe, O, N, and C in the Ti–Fe_2O_3/M–NC samples. Owing to the pronounced multiplet splitting characteristic of Fe *2p* core levels,[37] the Fe *2p* spectra (**Figure S2b**) were not deconvoluted; importantly, their overall spectral features remain essentially unchanged after M–NC loading, indicating that the electronic environment of Fe in Ti–Fe_2O_3 is not significantly perturbed by the incorporation of M–NC catalysts. High-resolution C *1s* spectra of pristine Ti–Fe_2O_3 (**Figure 1g**) were deconvoluted into four components corresponding to C–C, C–O, C=N–C, and O–C=O species. Upon incorporation of Ni–NC in Ti–Fe_2O_3/Ni–NC, broadened features were observed due to overlapping contributions from C–N and C–O bonds originating from the N-doped carbon framework of the M–NC catalyst. The corresponding N *1s* spectra of Ti–Fe_2O_3/Ni–NC and Ti–Fe_2O_3/Fe–NC (**Figure 1h**) exhibited four characteristic nitrogen species, assignable to pyridinic N, metal–N (M–N, M = Ni or Fe), pyrrolic N, and graphitic N, consistent with the formation of atomically dispersed M–N_x sites.[24] The presence of Ti in Ti–Fe_2O_3 was further confirmed by the Ti *2p* spectra shown in **Figure S2c**. There was no peak shift in both XPS (F**igure S2**) and Raman spectra (**Figure S3**) before and after the addition of Ni-CN, indicating that there is only physical contact between Ti-Fe_2O_3 and M-NC sheet. To directly verify the incorporation of Ni species, scanning transmission electron microscopy coupled with energy-dispersive X-ray spectroscopy (STEM–EDS) was performed. Elemental mapping (**Figures 1h-k**) confirmed the coexistence of Ni, N, and C in the Ni–NC catalyst, supporting the successful deposition of Ni–NC onto the Ti–Fe_2O_3 photoanode. Collectively, the XPS and STEM-EDS analyses confirmed the expected elemental composition and validated the successful construction of Ti–Fe_2O_3/M–NC hybrid photoanodes. Detailed atomic-scale characterization of the Fe–NC and Ni–NC catalyst powders prior to photoanode integration has been reported previously using high-angle annular dark-field STEM, energy-dispersive X-ray spectroscopy, X-ray absorption spectroscopy, time-of-flight secondary ion mass spectrometry (ToF-SIMS), and ^{57}Fe Mössbauer spectroscopy.[24, 25, 36] STEM–EDS and elemental mapping of Fe–NC are presented in **Figure S4**.

The PEC performance of the Ti–Fe_2O_3 photoanode was first evaluated in a stirred electrolyte containing 0.5 M glycerol and 1 M NaOH under 1 sun illumination (AM 1.5G, 100 mW cm^{-2}), using back-side illumination through the glass substrate. The current density–potential (*j–V*) curves recorded under chopped illumination are shown in **Figure 2a**, while the optimization of M–NC catalyst loading and glycerol concentration are presented in **Figure S5** and **Figure S6**. Pristine Ti–Fe_2O_3 delivered a photocurrent density of 0.8 mA cm^{-2} at +1.23 V_{RHE}. Upon modification with M–NC catalysts, the PEC activity was markedly enhanced. Ti–Fe_2O_3/Ni–NC exhibited a photocurrent density of 2.2 mA cm^{-2} at +1.23 V_{RHE}, corresponding to an approximately threefold increase relative to bare Ti–Fe_2O_3, while Ti–Fe_2O_3/Fe–NC achieved a photocurrent density of 1.9 mA cm^{-2} under the same conditions. To exclude

View Article Online
DOI: 10.1039/D6TA02778D

the influence of the N-containing carbon matrix alone, a control photoanode comprising Ti–Fe_2O_3 coated with NC (without Fe or Ni metal sites) was evaluated. This composite exhibited a substantially lower photocurrent density of 1.0 mA cm^{-2} at +1.23 V_{RHE} (**Figure S7a**), confirming that the enhanced activity originated from the presence of M–NC (M = Ni or Fe) rather than the NC support itself. Collectively, these results demonstrate that the incorporation of M–NC catalysts can effectively promote glycerol oxidation on Ti–Fe_2O_3 photoanodes. Incident photon-to-current efficiency (IPCE) measurements further corroborated these findings. As shown in **Figure 2b**, pristine Ti–Fe_2O_3 exhibited an IPCE of approximately 22% at 350 nm, whereas Ti–Fe_2O_3/Ni–NC and Ti–Fe_2O_3/Fe–NC achieved significantly higher IPCE values of approximately 58% and 55%, respectively, at the same wavelength. The enhanced IPCE across the UV–visible region confirmed that M–NC modification improved photon-to-current conversion efficiency, in good agreement with the trends observed in the *j–V* characteristics.

PEC GOR was performed at applied potentials of +0.8, +1.0, and +1.2 V_{RHE} for 2 h to analyze the liquid-phase oxidation products (**Figure 2c**). The SEM micrographs in **Figure S8** show the macro-scale morphologies of Ti–Fe_2O_3/Ni–NC and Ti–Fe_2O_3/Fe–NC remain intact after reaction. The effective reaction potential comprises the externally applied potential and the photovoltage generated by the hematite photoanode under illumination. Although the apparent photovoltage inferred from the shift in open-circuit potential was ~0.15 V, larger apparent potential shifts (>0.5 V) were typically observed at operating current densities, reflecting enhanced charge separation and interfacial kinetics under illumination and higher applied potentials.[35, 38] The major liquid-phase products, identified by high-performance liquid chromatography (HPLC), were glyceric acid (GLA), glycolic acid (GA), and formic acid (FA). Although the corresponding species formed under the PEC alkaline conditions were glycerate, glycolate, and formate, respectively, they are herein referred to by their acid forms for consistency with the literature and their commercial relevance after acidification. The production rates and selectivities of the oxidation products on different photoanodes at various applied potentials are summarized in **Figures 2c–d**. For all photoanodes, total product formation rates increased with increasing applied potential. At +0.8 V_{RHE}, pristine Ti–Fe_2O_3 predominantly produced GLA (~58% selectivity) and GA (~42% selectivity). Upon Ni–NC modification, the total production rate increased markedly, with product distribution strongly shifted toward GLA, reaching a selectivity of ~80%, highlighting the pronounced catalytic effect of Ni–NC. In contrast, Fe–NC loading also substantially enhanced the production rate but favored GA formation, achieving a selectivity of ~74% at the same potential. As the applied potential was increased from +0.8 to +1.2 V_{RHE}, both the production rate and product selectivity of pristine Ti–Fe_2O_3 remained largely unchanged. In contrast, Ti–Fe_2O_3/Ni–NC exhibited a pronounced evolution in product distribution, with the emergence of FA at higher potentials. The selectivity toward FA increased from 0% at +0.8 V_{RHE} to 49% at +1.2 V_{RHE}, indicating that either

View Article Online
DOI: 10.1039/D6TA02778D

the applied potential plays a critical role in steering product pathways in the presence of Ni–NC or that the oxidative conditions drive the dissolution and aggregation of Ni atoms into clusters, which have been shown to promote the C-C scission in glycerol oxidation towards formate.[39-41] To exclude contributions from the NC matrix, a Ti–Fe_2O_3/NC control photoanode was evaluated under identical conditions. It displayed similar production rates and selectivity to pristine Ti–Fe_2O_3 (**Figure S7b**), confirming that the observed selectivity modulation originated from the doped metal sites. In comparison, Ti–Fe_2O_3/Fe–NC maintained high selectivity toward GA with increasing potential, accompanied by enhanced production rates, while no FA formation was detected across the investigated potential range. Finally, calculated Faradaic efficiencies (FE) for liquid GLA, GA, and FA at different applied potentials are shown in **Figure S9**. At +0.8 V_{RHE}, the summation of these FEs reached 100%, confirming all the photocurrent observed is linked to glycerol oxidation to liquid products at this potential. However, at +1.0 and +1.2 V_{RHE}, some deviation from 100% was observed (e.g. 22% and 44% for Ti–Fe_2O_3/Ni–NC, respectively) suggesting competing gas evolution with increasing applied potentials. LSV measurements without glycerol (**Figure S5a**) consistently indicated increasing photocurrents with applied potential from +1.2 V_{RHE} for Ti–Fe_2O_3 and from +1.0 V_{RHE} for Ti–Fe_2O_3/Ni–NC. Based on the response of similar hematite systems, these photocurrents (and the deviation from 100% summation of GLA, GA, and FA FEs) at the highest applied potentials were assigned to mainly O_2 evolution.[35] A small contribution from complete glycerol oxidation to CO_2 gas at the highest applied potentials cannot be ruled out.

View Article Online
DOI: 10.1039/D6TA02778D

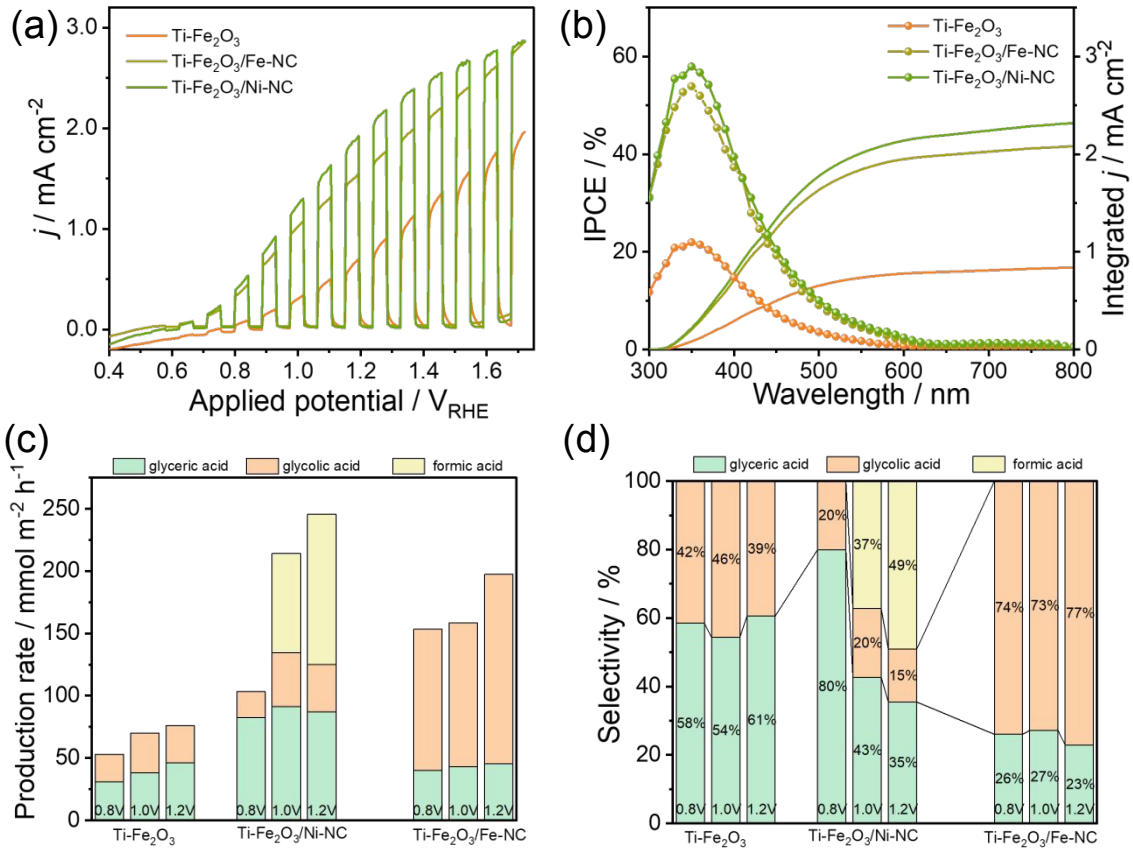

Figure 2. (a) (Photo)current–potential (*j–V*) curves of Ti–Fe_2O_3, Ti–Fe_2O_3/Fe–NC, and Ti–Fe_2O_3/Ni–NC photoanodes recorded under 1 sun illumination (Xe lamp, AM 1.5G filter, 100 mW cm^{-2}) with chopped light at a scan rate of 10 mV s^{-1} in 0.5 M glycerol and 1 M NaOH (pH = 13.7). (b) IPCE spectra measured at +1.23 V_{RHE} under monochromatic illumination (Xe lamp with monochromator) and corresponding integrated photocurrents for Ti–Fe_2O_3, Ti–Fe_2O_3/Ni–NC, and Ti–Fe_2O_3/Fe–NC. (c) Photoanodic production rates of glycerol oxidation products on different photoanodes at applied potentials of +0.8, +1.0, and +1.2 V_{RHE}. (d) Product selectivity toward glyceric acid (GLA), glycolic acid (GA), and formic acid (FA) under the corresponding conditions.

View Article Online
DOI: 10.1039/D6TA02778D

To investigate the evolution of active sites in M–NC catalysts at the minimal loadings employed in the photoanodes, highly surface-sensitive ToF-SIMS was performed on fresh and post-reaction Ti–Fe_2O_3/M–NC photoanodes, focusing on the detection of NiN_xC_y fragments. Fe–NC was not examined by ToF-SIMS, as previous studies have reported no observable FeN_xC_y fragments in this catalyst, likely due to the lower ionization efficiency of Fe-containing species.[25] Measurements were conducted in negative ion mode to enhance the ionization yield of NiN_xC_y fragments generated by bond-cleavage events induced by the negative primary ion beam.[42] A bare NC sample was also analyzed as a reference to aid fragment assignment and distinguish Ni-derived species from other surface contaminants. Quantitative comparison was enabled through algebraic deconvolution of overlapping ^{58}Ni and ^{60}Ni isotopic fragments following previously reported methods.[25, 42] The detected NiN_xC_y fragments (**Figure 3a–c**) were consistent with atomically dispersed Ni species within N-containing carbon, in agreement with prior characterization of these materials.[25] Importantly, no m/z signals corresponding to dinuclear Ni species ($Ni_2N_xC_y^-$) were detected, suggesting the absence of detectable Ni–Ni aggregation. Interestingly, normalized NiN_xC_y fragment intensities were lower for fresh photoanodes and increased after PEC GOR testing (**Figure 3c**), which may have resulted from surface cleaning during operation or changes in surface chemistry, such as adsorption of electrolyte-derived species that enhance fragment ionization. Calibration and reference peak intensities of the NC-related peaks, including C^-, C_2^-, C_4^-, and C_6^- in **Figure S10a**, as well as $Fe_2O_3^-$ in **Figures 3a–b**, remained comparable before and after testing, although the slightly lower NC peak intensities in the post-reaction sample indicate minor NC degradation during oxidation. In addition, the increased $KHCO_3^-$ signal (**Figure S10b)** indicated the presence of residual electrolyte species on the post-reaction samples. The relevant fragment mapping counts showed that the Ni-NC was well dispersed on the surface of Ti-Fe_2O_3 (**Figure S11**). While ToF-SIMS revealed enhanced NiN_xC_y signals after PEC operation, it has been recently established that M–NC can undergo oxidation and structural reconstruction under anodic potentials.[29] According to the Ni Pourbaix diagram, Ni readily oxidizes to higher-valence species (e.g., NiOOH/$Ni(OH)_2$ or Ni_2O_3/NiO_2) at pH ≈ 14 and ≈ +1 V_{SHE} (10^{-6} mol L^{-1}),[43] and such transformations may involve partial aggregation into small (oxy)hydroxide clusters featuring M–O–M or M–O–M′ (M/M′ = Fe or Ni) linkages.[29, 43] To further assess the dispersion and structural integrity of Ni sites, high-resolution transmission electron microscopy (HRTEM) and STEM–EDS were employed. For fresh Ti–Fe_2O_3/Ni–NC photoanodes, STEM–EDS mapping (**Figure 3d**) revealed uniformly distributed Ni and N signals alongside Fe from the Ti–Fe_2O_3 substrate, while aberration-corrected HAADF-STEM (**Figure 3e**) confirmed atomic-level dispersion of Ni sites. Following a 28 h stability test at +1.23 V_{RHE} under 1 sun illumination (**Figure S12**), Ti–Fe_2O_3/Ni–NC retained approximately 82% of its initial photocurrent, indicating operational durability. Post-reaction STEM–EDS mapping (**Figure 3f**) and atomic-resolution imaging (**Figure 3g**) showed a reduced Ni signal associated with the NC relative to fresh samples as well as the presence of Ni-rich particles, suggesting the partial oxidation and aggregation of Ni single-atom sites during PEC

View Article Online
DOI: 10.1039/D6TA02778D

GOR, which may have contributed both to the observed photocurrent decay during prolonged operation and to the shift in product distribution towards formate at high anodic potentials.[39, 40]

The atomic structure of the Ti–Fe_2O_3/M–NC (M = Ni or Fe) photoanode is illustrated in **Figure 3h**, while the corresponding energy band alignment of the individual components prior to contact is schematically shown in **Figure 3i**. Ti–Fe_2O_3 exhibits a work function of approximately −4.1 eV,[35] corresponding to a relatively shallow Fermi level compared with that of M–NC (−5.31 eV for Ni–NC and −5.29 eV for Fe–NC).[44, 45] Upon contact between Ti–Fe_2O_3 and M–NC, Fermi-level equilibration is expected to occur, leading to upward band bending in the Ti–Fe_2O_3 near the interface with M–NC (**Figure 3j**). This interfacial energy-level alignment is characteristic of a Schottky junction, generating a built-in electric field that promotes charge-carrier separation and facilitates hole transfer from Ti–Fe_2O_3 toward the M–NC layer. Such a charge-transfer configuration is consistent with the enhanced photocurrent densities observed for Ti–Fe_2O_3/M–NC photoanodes (**Figure 2a**).[46] Under illumination, photogenerated holes in Ti–Fe_2O_3 preferentially migrate toward the M–NC component, where they can participate in interfacial glycerol oxidation reactions at the M–NC/electrolyte interface.[46] However, care must be taken to avoid high potentials where photogenerated holes could also contribute to partial self-oxidation of the carbon framework.[47]

View Article Online
DOI: 10.1039/D6TA02778D

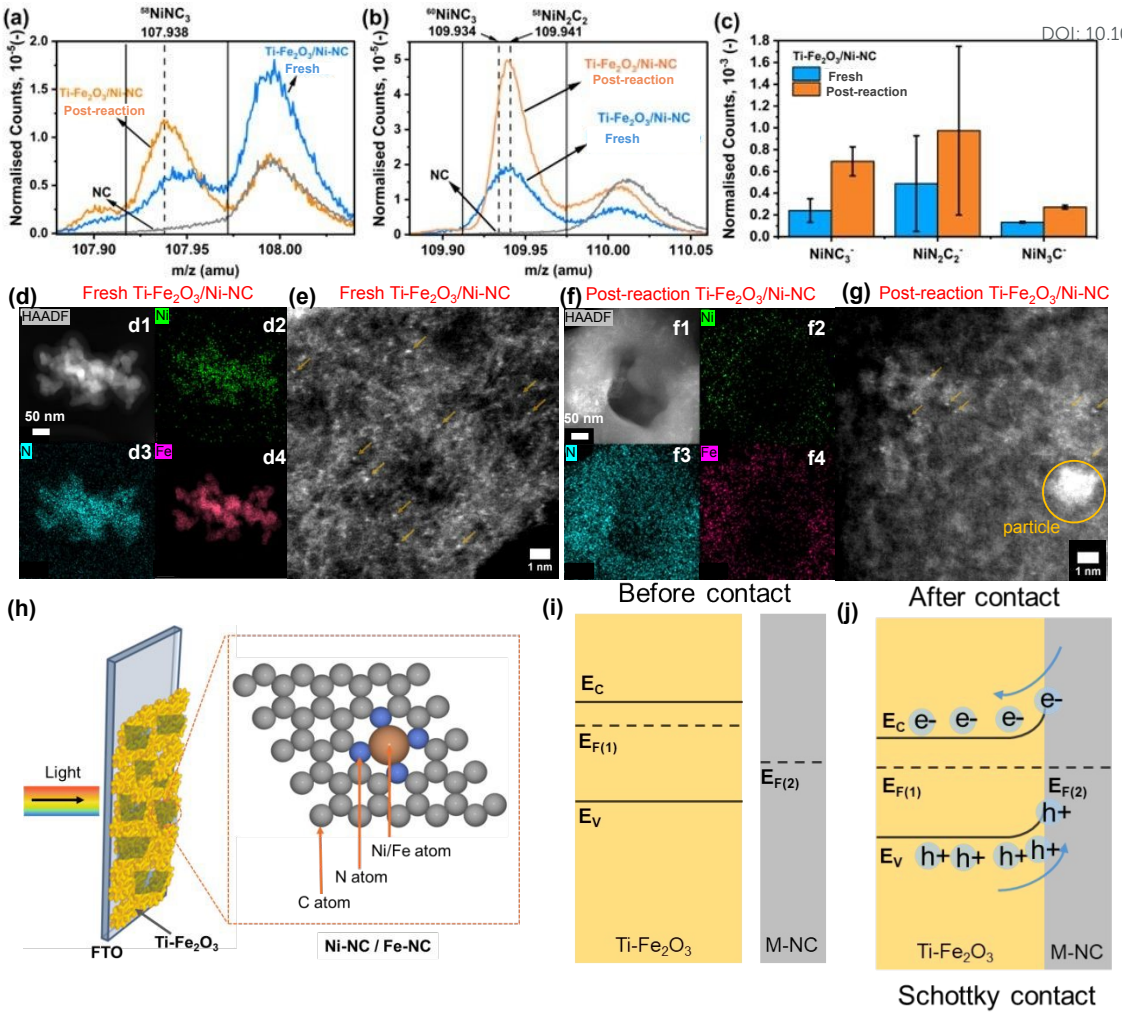

Figure 3. (a–c) Negative-polarity ToF-SIMS analysis of fresh and post-tested Ti–Fe_2O_3/Ni–NC photoanodes after PEC operation for 2 h at +1.23 V_{RHE} in 0.5 M glycerol and 1 M NaOH under 1 sun illumination. Fragment ion counts, normalized to total ion counts, for mass spectral regions assigned to $^{58}NiNC_3^-$, $^{60}NiNC_3^-$/$^{58}NiN_2C_2^-$, and identified major $^{58}NiN_xC_y^-$ fragments. The bars represent the mean values, and the error bars the deviation of two distinct measurements at locations where Ni–NC was visibly deposited. (d) STEM–EDS elemental mapping of fresh Ti–Fe_2O_3/Ni–NC. Scale bars are identical for all panels in d. (e) HAADF-STEM micrograph of fresh Ni–NC. (f) STEM–EDS elemental mapping of Ti–Fe_2O_3/Ni–NC after PEC operation at +1.23 V_{RHE} for 28 h under 1 sun illumination in 0.5 M glycerol and 1 M NaOH. Scale bars are identical for all panels in f. (g) HAADF-STEM micrograph of used Ni–NC. (h) Schematic illustration of the Ti–Fe_2O_3/M–NC (M = Ni or Fe) photoanode and the atomic structure of M–NC. (i, j) Schematic energy band diagrams of the Ti–Fe_2O_3/M–NC photoanode before and after contact.

View Article Online
DOI: 10.1039/D6TA02778D

To rationalize the experimentally observed differences in glycerol oxidation product selectivity between Ti–Fe_2O_3/Ni–NC and Ti–Fe_2O_3/Fe–NC photoanodes, DFT calculations were performed to evaluate the energetics of glycerol electro-oxidation intermediates and reaction pathways. The modeled catalyst surface consisted of a metal–N_4–pyridine-doped graphene structure, representing Ni–NC or Fe–NC, as shown in **Figure 3h**. Glycerol oxidation was modeled as described elsewhere,[48] in which two reaction types [dehydrogenation and hydroxyl (OH) incorporation] were considered for each elementary oxidation step (described in the Computational Section of the Supporting Information). All possible intermediates evaluated at each step are summarized in **Table S3–S4**, and the reaction pathways constructed from the most stable intermediates at $U_{\text{vs RHE}} = 0$V are presented in **Figures 4a–b**. Owing to model limitations, including the exclusion of the Ti–Fe_2O_3 photoactive component and solvation effects, the predicted final products did not exactly reproduce experimental observations; nevertheless, the calculations provided valuable mechanistic insights into metal-dependent oxidation activity and pathway energetics.

The DFT results indicated that Fe–NC should exhibit intrinsically higher glycerol oxidation activity than Ni–NC. For Ni–NC, the potential-determining step was the initial glycerol dehydrogenation step, in which $C_3H_8O_3$ was oxidized to $CH_2OH–CHOH–CH_2O$*, requiring a minimum potential of +1.24 V_{RHE} to become thermodynamically favorable [unlike Ni(111), which shows favorable glycerol electro oxidation even at 0 V_{RHE}[49,43]]. Above this +1.24 V_{RHE} threshold, all subsequent reaction steps were downhill in free energy, enabling multiple reaction pathways (**Table S4**), which was consistent with the experimentally observed formation of multiple oxidation products (GLA, GA, and FA), even though specific products were not explicitly predicted by the model. In contrast, Fe–NC required a significantly lower activation potential of only +0.22 V_{RHE} for the initial glycerol dehydrogenation step, nearly 1 V lower than that of Ni–NC, highlighting its superior intrinsic oxidation activity. For Fe–NC, the potential-determining step occurred at the fourth oxidation step, where $CH_2OH–CO–$*$CHOH$ is oxidized to $CH_2OH–CO–CHO$, with a calculated ΔG ranging from 0.43 to 0.76 eV. Once the potential exceeded +0.33 V_{RHE}, all six oxidation steps became thermodynamically downhill, facilitating rapid glycerol oxidation.

Experimentally, FA was observed during glycerol photoanodic oxidation on Ti–Fe_2O_3/Ni–NC but not on Ti–Fe_2O_3/Fe–NC (**Figures 2c–d**). To elucidate this discrepancy, the electro-oxidation pathways of FA were further examined on both Ni–NC and Fe–NC catalysts. Two reaction mechanisms (dehydrogenation and OH incorporation) were again considered, with all possible intermediates listed in **Tables S5–S6**. The resulting pathways constructed from the most stable intermediates at 0 V_{RHE} are shown in **Figures 4c–d**. On Fe–NC, both oxidation steps for FA were thermodynamically favorable (downhill), indicating that FA was readily oxidized to CO_2 and therefore did not accumulate to

View Article Online
DOI: 10.1039/D6TA02778D

detectable levels. In contrast, on Ni–NC, the first oxidation step of FA to HCOO* was endergonic with ΔG = 0.75 eV, requiring a potential of at least 0.75 V_{RHE} to proceed, allowing FA to persist under reaction conditions, consistent with its experimental detection on Ti–Fe_2O_3/Ni–NC. These results highlighted the higher intrinsic oxidation activity of Fe–NC relative to Ni–NC and provided a mechanistic explanation for the observed metal-dependent product selectivity.

View Article Online
DOI: 10.1039/D6TA02778D

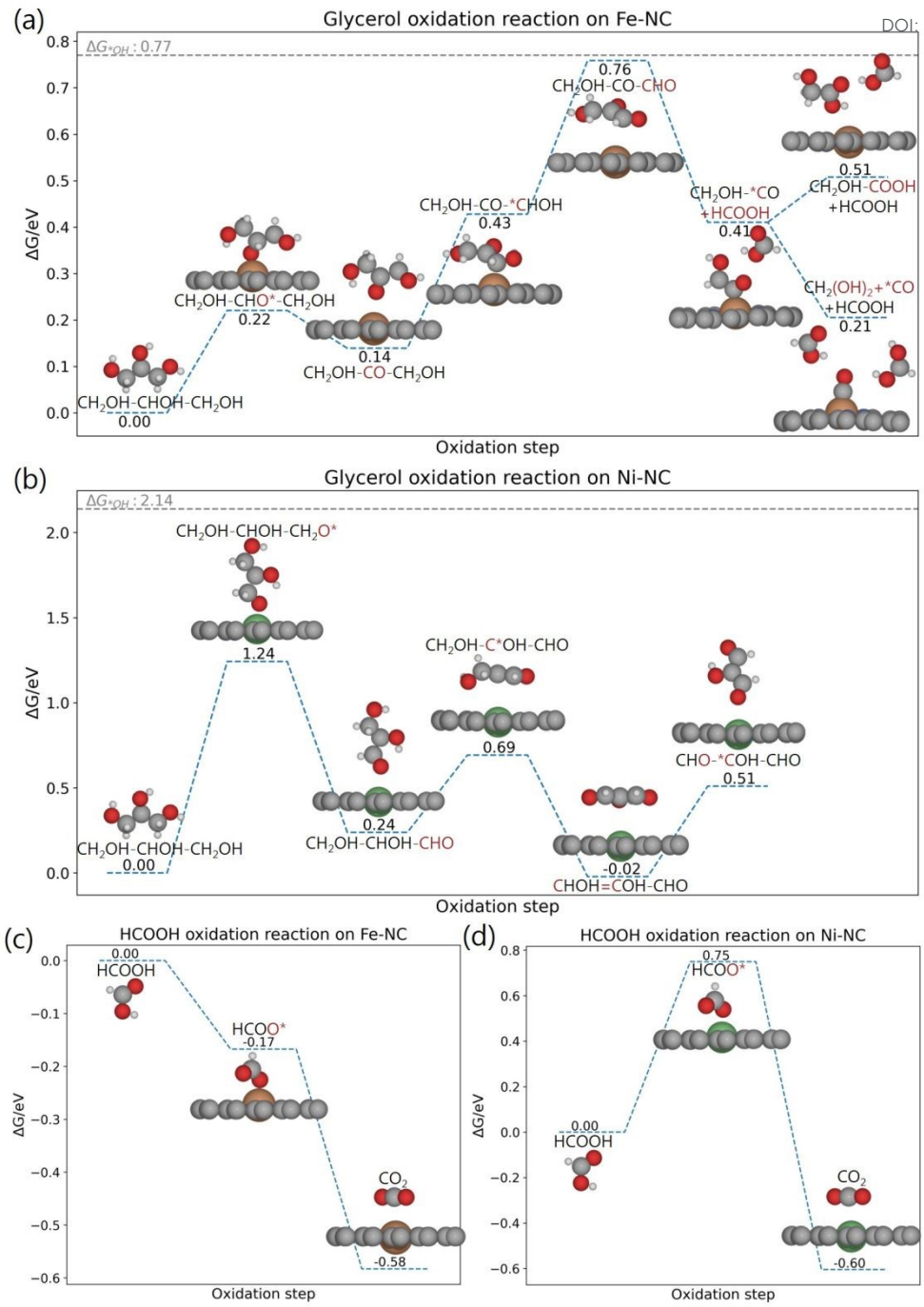

Figure 4. Free-energy diagrams for possible electro-oxidation pathways of (a, b) glycerol and (c, d) formic acid (FA) on Fe–NC and Ni–NC catalysts evaluated at $U_{\mathrm{vs\,RHE}} = 0$ V: (a) glycerol on Fe–NC, (b) glycerol on Ni–NC, (c) FA on Fe–NC, and (d) FA on Ni–NC.

Based on the above results and discussion, a proposed mechanism for solar-driven glycerol oxidation over Ti–Fe_2O_3/M–NC (M = Fe or Ni) hybrid photoanodes is illustrated in **Figure 5**. Under light irradiation, photogenerated holes (h^+) in Ti–Fe_2O_3 migrate toward the M–NC cocatalyst driven by the built-in electric field at the Ti–Fe_2O_3/M–NC Schottky junction. These holes subsequently reach the M–

View Article Online
DOI: 10.1039/D6TA02778D

NC/electrolyte interface, where glycerol oxidation occurs. Fe–NC exhibits intrinsically higher glycerol oxidation activity than Ni–NC. For Ni–NC, the potential-determining step is the initial glycerol dehydrogenation step, in which $C_3H_8O_3$ is oxidized to $CH_2OH–CHOH–CH_2O^*$. Once this step is overcome, all subsequent reaction steps are thermodynamically downhill, enabling multiple reaction pathways and leading to the formation of various oxidation products, including GLA, GA, and FA. In contrast, for Fe–NC, the potential-determining step occurs at the fourth oxidation step, where $CH_2OH–CO–^*CHOH$ is oxidized to $CH_2OH–CO–CHO$. All six oxidation steps become thermodynamically downhill at significantly lower potentials than Ni–NC, facilitating faster glycerol oxidation and favoring selective GLA formation. Meanwhile, photogenerated electrons (e^-) are extracted from the photoanode and driven through the external circuit by the applied potential, with charge balance maintained by the potentiostat, resulting in electron delivery to the Pt counter electrode where the hydrogen evolution reaction occurs.

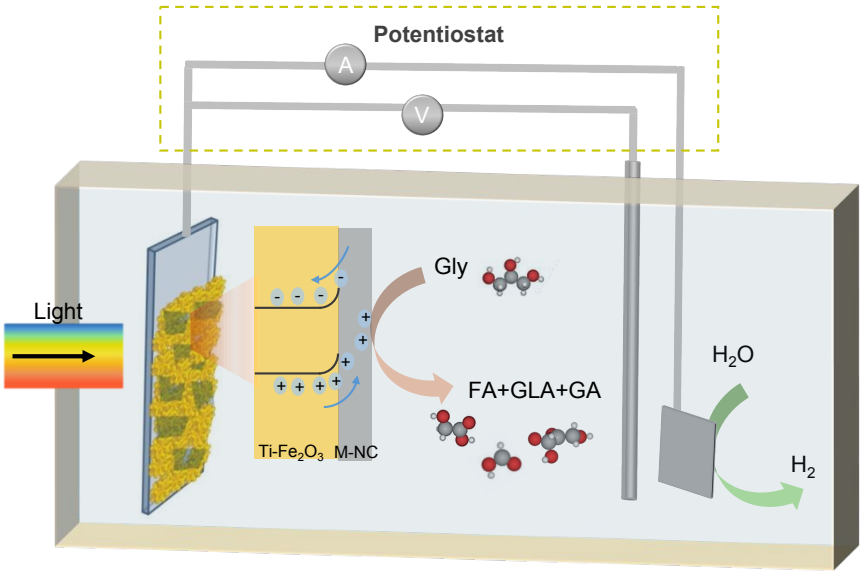

Figure 5. Schematic illustration of the photoinduced charge transfer and reaction mechanism for PEC glycerol oxidation over Ti–Fe_2O_3/M–NC (M = Fe or Ni) hybrid photoanodes.

View Article Online
DOI: 10.1039/D6TA02778D

3 Conclusions

Ti–Fe_2O_3/M–NC (M = Fe or Ni) hybrid photoanodes were successfully developed to address the key challenges of low activity, inefficient charge separation, and limited selectivity control in photoelectrochemical glycerol oxidation (PEC GOR). The integration of single-atom M–NC cocatalysts with Ti–Fe_2O_3 provides two principal advantages. First, the formation of a Schottky junction at the Ti–Fe_2O_3/M–NC interface establishes a built-in electric field that promotes efficient charge-carrier separation and directional hole transfer, resulting in a substantial enhancement of photocurrent density, reaching up to 2.2 mA cm^{-2} for Ti–Fe_2O_3/Ni–NC at +1.23 V_{RHE}. Second, the use of different M–NC catalysts enables modulation of product selectivity, with Ni–NC favoring glyceric acid formation (~80% selectivity) and Fe–NC preferentially promoting glycolic acid production (~74% selectivity) at +0.8 V_{RHE}, while maintaining stable or tunable performance across a broad potential window (+0.8 to +1.2 V_{RHE}). Density functional theory calculations reveal that the distinct selectivity trends observed for Ni–NC and Fe–NC originate from their intrinsic differences in oxidation activity, providing a mechanistic foundation for the experimentally observed product distributions and supporting the proposed selective PEC GOR pathways. Post-reaction analyses using ToF-SIMS and HAADF-STEM show that the Ni single-atom metal sites largely retain their dispersion after extended operation at +1.23 V_{RHE}. However, partial Ni oxidation to nanoclusters is evident, which can also explain the selectivity change of Ti–Fe_2O_3/Ni–NC to formic acid at these potentials. Increasing photocurrents with applied potential in the absence of glycerol and Faradaic efficiencies indicate competing gas evolution at the higher applied potentials. Overall, this work advances the rational design of a selective photoanodes for biomass valorization by exploiting the structural and electronic synergy between hematite photoanodes and single-atom M–NC cocatalysts and extends the application of single-atom catalysts to solar-driven PEC energy conversion.

Conflicts of interest

There are no conflicts to declare.

Acknowledgements

The authors thank the Department of Chemical Engineering at Imperial College London for funding a Ph.D. scholarship for M.Y. S.E. acknowledges financial support from the UK Engineering and Physical Sciences Research Council (EPSRC) through grant EP/S030727/1. J.B. acknowledges financial support

View Article Online
DOI: 10.1039/D6TA02778D

from Imperial College London via the Imperial College Research Fellowship (ICRF) scheme. A.P. thanks the EPSRC Doctoral Prize Fellowship (EP/W524323/1). Z.M., H.H.K., and J.R. acknowledge financial support from the Independent Research Fund Denmark grant no. 1127-00372B and the Danish National Research Foundation, Center for High Entropy Alloy Catalysis (CHEAC) DNRF149. SJH acknowledges funding from EPSRC grant EP/Y024303/1. TEM/STEM was supported by the Royce Institute for Advanced Materials, funded through EPSRC grants EP/R00661X/1, EP/S019367/1, EP/P025021/1 and EP/P025498/1.

References

1. Chen, W.; Zhang, L.; Xu, L.; He, Y.; Pang, H.; Wang, S.; Zou, Y., Pulse potential mediated selectivity for the electrocatalytic oxidation of glycerol to glyceric acid. *Nature Communications* **2024,** *15* (1), 2420.

2. Sheng, H.; Janes, A. N.; Ross, R. D.; Hofstetter, H.; Lee, K.; Schmidt, J. R.; Jin, S., Linear paired electrochemical valorization of glycerol enabled by the electro-Fenton process using a stable NiSe2 cathode. *Nature Catalysis* **2022,** *5* (8), 716-725.

3. Miao, Y.; Li, Z.; Shao, M., Photoelectrochemical Glycerol Oxidation Coupled with Hydrogen Production. *ChemCatChem* **2024,** *16* (5), e202301321.

4. Su, K.; Chen, H.; Ren, S.; Gao, R.-T.; Wu, L.; Wang, L., Unbiased Stable Photoelectrochemical Glycerol Oxidation on Hematite Photoanodes. *Angewandte Chemie International Edition* **2025,** *64* (38), e202509062.

5. Liu, Y.; Shang, H.; Zhang, B.; Yan, D.; Xiang, X., Surface fluorination of BiVO4 for the photoelectrochemical oxidation of glycerol to formic acid. *Nature Communications* **2024,** *15* (1), 8155.

6. Pulignani, C.; Mesa, C. A.; Hillman, S. A. J.; Uekert, T.; Giménez, S.; Durrant, J. R.; Reisner, E., Rational Design of Carbon Nitride Photoelectrodes with High Activity Toward Organic Oxidations. *Angewandte Chemie* **2022,** *134* (50), e202211587.

7. Sivula, K.; Le Formal, F.; Grätzel, M., Solar Water Splitting: Progress Using Hematite (α-Fe2O3) Photoelectrodes. *ChemSusChem* **2011,** *4* (4), 432-449.

8. Jang, J.-H.; Chaule, S.; Kang, J., Chapter 13 - Hematite (α-Fe2O3) as a solar energy harvesting photoanode for photo-electrochemical (PEC) water splitting. In *Photoelectrochemical Engineering for Solar Harvesting*, Kazim, S.; Tahir, M. N.; Ahmad, S.; Mathur, S., Eds. Elsevier: 2024; pp 373-404.

9. Li, Y.; Kim, J.; Hong, W. T.; Kim, J. Y.; Lei, Q.; Han, H.; Baeck, U.; Kim, D. H.; Choi, C. H.; Kim, B.-H.; Chung, C.-H.; Kim, J. K., Highly Selective Photoelectrochemical Glycerol Valorization toward Lactic Acid with Low-Valence Bimetallic Overlayer on CuWO4. *ACS Energy Letters* **2025,** *10* (5), 2305-2314.

10. Luo, H.; Barrio, J.; Sunny, N.; Li, A.; Steier, L.; Shah, N.; Stephens, I. E. L.; Titirici, M.-M., Progress and Perspectives in Photo- and Electrochemical-Oxidation of Biomass for Sustainable Chemicals and Hydrogen Production. *Advanced Energy Materials* **2021,** *11* (43), 2101180.

11. Huang, X.; Perera, I. P.; Shubhashish, S.; Suib, S. L., Unveiling Enhanced PEC Water Oxidation: Morphology Tuning and Interfacial Phase Change in α-Fe2O3@K-OMS-2 Branched Core–Shell Nanoarrays. *ACS Applied Materials & Interfaces* **2024,** *16* (19), 24712-24722.

12. Morales, D. M.; Jambrec, D.; Kazakova, M. A.; Braun, M.; Sikdar, N.; Koul, A.; Brix, A. C.; Seisel, S.; Andronescu, C.; Schuhmann, W., Electrocatalytic Conversion of Glycerol to Oxalate on Ni Oxide Nanoparticles-Modified Oxidized Multiwalled Carbon Nanotubes. *ACS Catalysis* **2022,** *12* (2), 982-992.

13. Song, M.; Bai, Y.; Li, J.; Qi, X., Efficient strategies for the preparation of non-noble metal catalysts for electrocatalytic glycerol oxidation towards high-value-added chemicals. *RSC advances* **2025,** *15* (26), 20513-20529.

14. Mitchell, S.; Pérez-Ramírez, J., Single atom catalysis: a decade of stunning progress and the promise for a bright future. *Nature Communications* **2020,** *11* (1), 4302.

15. Guo, J.; Liu, H.; Li, D.; Wang, J.; Djitcheu, X.; He, D.; Zhang, Q., A minireview on the synthesis of single atom catalysts. *RSC Advances* **2022,** *12* (15), 9373-9394.

16. Feng, X.; Sun, T.; Feng, X.; Yu, H.; Yang, Y.; Chen, L.; Zhang, F., Single-Atomic-Site Platinum Steers Middle Hydroxyl Selective Oxidation on Amorphous/Crystalline Homojunction for Photoelectrochemical Glycerol Oxidation Coupled with Hydrogen Generation. *Advanced Functional Materials* **2024,** *34* (26), 2316238.

17. Liu, L.; Corma, A., Metal catalysts for heterogeneous catalysis: from single atoms to nanoclusters and nanoparticles. *Chemical reviews* **2018,** *118* (10), 4981-5079.

18. Cherevko, S.; Zeradjanin, A. R.; Keeley, G. P.; Mayrhofer, K. J. J., A Comparative Study on Gold and Platinum Dissolution in Acidic and Alkaline Media. *Journal of The Electrochemical Society* **2014,** *161* (12), H822.

19. Guo, Q.; Zhao, Q.; Crespo-Otero, R.; Di Tommaso, D.; Tang, J.; Dimitrov, S. D.; Titirici, M.-M.; Li, X.; Jorge Sobrido, A. B., Single-Atom Iridium on Hematite Photoanodes for Solar Water Splitting: Catalyst or Spectator? *Journal of the American Chemical Society* **2023,** *145* (3), 1686-1695.

20. Menga, D.; Low, J. L.; Li, Y.-S.; Arčon, I.; Koyutürk, B.; Wagner, F.; Ruiz-Zepeda, F.; Gaberščček, M.; Paulus, B.; Fellinger, T.-P., Resolving the Dilemma of Fe–N–C Catalysts by the Selective Synthesis of Tetrapyrrolic Active Sites via an Imprinting Strategy. *Journal of the American Chemical Society* **2021,** *143* (43), 18010-18019.

21. Yin, S.; Yi, H.; Liu, M.; Yang, J.; Yang, S.; Zhang, B.-W.; Chen, L.; Cheng, X.; Huang, H.; Huang, R.; Jiang, Y.; Liao, H.; Sun, S., An in situ exploration of how Fe/N/C oxygen reduction catalysts evolve during synthesis under pyrolytic conditions. *Nature Communications* **2024,** *15* (1), 6229.

22. Mehmood, A.; Pampel, J.; Ali, G.; Ha, H. Y.; Ruiz-Zepeda, F.; Fellinger, T.-P., Facile Metal Coordination of Active Site Imprinted Nitrogen Doped Carbons for the Conservative Preparation of Non-Noble Metal Oxygen Reduction Electrocatalysts. *Advanced Energy Materials* **2018,** *8* (9), 1701771.

23. Menga, D.; Ruiz-Zepeda, F.; Moriau, L.; Šala, M.; Wagner, F.; Koyutürk, B.; Bele, M.; Petek, U.; Hodnik, N.; Gaberščček, M.; Fellinger, T.-P., Active-Site Imprinting: Preparation of Fe–N–

C Catalysts from Zinc Ion–Templated Ionothermal Nitrogen-Doped Carbons. *Advanced Energy Materials* **2019,** *9* (43), 1902412.

24. Liu, S.; Mukadam, Z.; Pedersen, A.; Barrio, J.; Parker, J.; Tyrrell, H.; Haigh, S. J.; Titirici, M. M.; Stephens, I. E. L.; Kastlunger, G., Bridging Outer- and Inner-Sphere Electrosynthesis from Biomass-Derived Furfural Using Single Atom Catalysts. *The Journal of Physical Chemistry C* **2025,** *129* (10), 5032-5042.

25. Sarma, S. C.; Barrio, J.; Bagger, A.; Pedersen, A.; Gong, M.; Luo, H.; Wang, M.; Favero, S.; Zhao, C.-X.; Zhang, Q.; Kucernak, A.; Titirici, M.-M.; Stephens, I. E. L., Reaching the Fundamental Limitation in CO2 Reduction to CO with Single Atom Catalysts. *Advanced Functional Materials* **2023,** *33* (41), 2302468.

26. Braga, D. S.; Pedersen, A.; Riyaz, M.; Barrio, J.; Bagger, A.; Neckel, I. T.; Mariano, T. M.; Winkler, M. E.; Stephens, I. E.; Titirici, M. M., In situ structural evolution and activity descriptor of atomically dispersed catalysts during nitrate electroreduction. **2025,** 12 (39), e10282.

27. Mehmood, A.; Gong, M.; Jaouen, F.; Roy, A.; Zitolo, A.; Khan, A.; Sougrati, M.-T.; Primbs, M.; Bonastre, A. M.; Fongalland, D.; Drazic, G.; Strasser, P.; Kucernak, A., High loading of single atomic iron sites in Fe–NC oxygen reduction catalysts for proton exchange membrane fuel cells. *Nature Catalysis* **2022,** *5* (4), 311-323.

28. Dresp, S.; Luo, F.; Schmack, R.; Kühl, S.; Gliech, M.; Strasser, P., An efficient bifunctional two-component catalyst for oxygen reduction and oxygen evolution in reversible fuel cells, electrolyzers and rechargeable air electrodes. *Energy & Environmental Science* **2016,** *9* (6), 2020-2024.

29. Wan, W.; Kang, L.; Schnegg, A.; Ruediger, O.; Chen, Z.; Allen, C. S.; Liu, L.; Chabbra, S.; DeBeer, S.; Heumann, S., Carbon-Supported Single Fe/Co/Ni Atom Catalysts for Water Oxidation: Unveiling the Dynamic Active Sites. *Angewandte Chemie International Edition* **2025,** *n/a* (n/a), e202424629.

30. Ku, Y.-P.; Kumar, K.; Hutzler, A.; Götz, C.; Vorochta, M.; Sougrati, M. T.; Lloret, V.; Ehelebe, K.; Mayrhofer, K. J. J.; Thiele, S.; Khalakhan, I.; Böhm, T.; Jaouen, F.; Cherevko, S., Impact of Carbon Corrosion and Denitrogenation on the Deactivation of Fe–N–C Catalysts in Alkaline Media. *ACS Catalysis* **2024,** *14* (11), 8576-8591.

31. Zhao, K.; Han, S.; Ke, L.; Wu, X.; Yan, X.; Cao, X.; Li, L.; Jiang, X.; Wang, Z.; Liu, H.; Yan, N., Operando Studies of Electrochemical Denitrogenation and Its Mitigation of N-Doped Carbon Catalysts in Alkaline Media. *ACS Catalysis* **2023,** *13* (5), 2813-2821.

32. Möller, S.; Barwe, S.; Masa, J.; Wintrich, D.; Seisel, S.; Baltruschat, H.; Schuhmann, W., Online Monitoring of Electrochemical Carbon Corrosion in Alkaline Electrolytes by Differential Electrochemical Mass Spectrometry. *Angewandte Chemie International Edition* **2020,** *59* (4), 1585-1589.

33. Ji, S. G.; Kim, H.; Lee, W. H.; Oh, H.-S.; Choi, C. H., Real-time monitoring of electrochemical carbon corrosion in alkaline media. *Journal of Materials Chemistry A* **2021,** *9* (35), 19834-19839.

34. Franceschi, G.; Kraushofer, F.; Meier, M.; Parkinson, G. S.; Schmid, M.; Diebold, U.; Riva, M., A Model System for Photocatalysis: Ti-Doped α-Fe2O3(1$\bar{1}$02) Single-Crystalline Films. *Chemistry of Materials* **2020,** *32* (9), 3753-3764.

35. Yang, M.; Oldham, L. I.; Daboczi, M.; Baghdadi, Y.; Cui, J.; Benetti, D.; Zhang, W. Durrant, J. R.; Hankin, A.; Eslava, S., Advancing Hematite Photoanodes for Photoelectrochemical Water Splitting: The Impact of g-C3N4 Supported Ni-CoP on Photogenerated Hole Dynamics. *Advanced Energy Materials* **2024,** *14* (29), 2401298.

36. Barrio, J.; Pedersen, A.; Sarma, S. C.; Bagger, A.; Gong, M.; Favero, S.; Zhao, C.-X.; Garcia-Serres, R.; Li, A. Y.; Zhang, Q.; Jaouen, F.; Maillard, F.; Kucernak, A.; Stephens, I. E. L.; Titirici, M.-M., FeNC Oxygen Reduction Electrocatalyst with High Utilization Penta-Coordinated Sites. *Advanced Materials* **2023,** *35* (14), 2211022.

37. Grosvenor, A. P.; Kobe, B. A.; Biesinger, M. C.; McIntyre, N. S., Investigation of multiplet splitting of Fe 2p XPS spectra and bonding in iron compounds. *Surface and Interface Analysis* **2004,** *36* (12), 1564-1574.

38. Le Formal, F.; Sivula, K.; Grätzel, M., The Transient Photocurrent and Photovoltage Behavior of a Hematite Photoanode under Working Conditions and the Influence of Surface Treatments. *The Journal of Physical Chemistry C* **2012,** *116* (51), 26707-26720.

39. Ng, E.; Mesa, C. A.; Más-Marzá, E.; Giménez, S., Current-Dependent Product Distribution and Reaction Mechanisms of Glycerol Electrooxidation on Nickel. *ChemElectroChem* **2025,** *12* (3), e202400534.

40. Oliveira, V. L.; Morais, C.; Servat, K.; Napporn, T. W.; Tremiliosi-Filho, G.; Kokoh, K. B., Glycerol oxidation on nickel based nanocatalysts in alkaline medium – Identification of the reaction products. *Journal of Electroanalytical Chemistry* **2013,** *703*, 56-62.

41. Chen, W.; Shi, J.; Xie, C.; Zhou, W.; Xu, L.; Li, Y.; Wu, Y.; Wu, B.; Huang, Y. C.; Zhou, B.; Yang, M.; Liu, J.; Dong, C. L.; Wang, T.; Zou, Y.; Wang, S., Unraveling the electrophilic oxygen-mediated mechanism for alcohol electrooxidation on NiO. *Natl Sci Rev* **2023,** *10* (5), nwad099.

42. Koshy, D. M.; Landers, A. T.; Cullen, D. A.; Ievlev, A. V.; Meyer Iii, H. M.; Hahn, C.; Bao, Z.; Jaramillo, T. F., Direct Characterization of Atomically Dispersed Catalysts: Nitrogen-Coordinated Ni Sites in Carbon-Based Materials for CO2 Electroreduction. *Advanced Energy Materials* **2020,** *10* (39), 2001836.

43. Huang, L. F.; Hutchison, M. J.; Santucci, R. J., Jr.; Scully, J. R.; Rondinelli, J. M., Improved Electrochemical Phase Diagrams from Theory and Experiment: The Ni–Water System and Its Complex Compounds. *The Journal of Physical Chemistry C* **2017,** *121* (18), 9782-9789.

44. Meng, X.; Chen, S.; Hong, S.; Zheng, L.; Liu, X.; Shi, G.; Bielawski, C. W.; Geng, J., Using the fermi level as a predictive indicator of the electrocatalytic activities displayed by single-atom catalysts in sulfur cathode reactions. *Chemical Engineering Journal* **2024,** *486*, 150241.

45. Glasoe, G. N., Contact Potential Difference between Iron and Nickel and their Photoelectric Work Functions. *Physical Review* **1931,** *38* (8), 1490-1496.

46. Cui, J.; Daboczi, M.; Cui, Z.; Gong, M.; Flitcroft, J.; Skelton, J.; Parker, S. C.; Eslava, S., BiVO4 Photoanodes Enhanced with Metal Phosphide Co-Catalysts: Relevant Properties to Boost Photoanode Performance. *Small* **2024,** *20* (7), 2306757.

47. Antoine, O.; Augustynski, J., Photo-electrochemical behaviour of glassy carbon. *Electrochemistry Communications* **2001,** *3* (4), 195-198.

48. Meng, Z.; Tran, D.; Hjelm, J.; Kristoffersen, H. H.; Rossmeisl, J., Insight into Selectivity Differences of Glycerol Electro-Oxidation on Pt(111) and Ag(111). *ACS Catalysis* **2024,** *14* (4), 2455-2462.

49. Valter, M.; dos Santos, E. C.; Pettersson, L. G. M.; Hellman, A., Partial Electrooxidation of Glycerol on Close-Packed Transition Metal Surfaces: Insights from First-Principles Calculations. *The Journal of Physical Chemistry C* **2020,** *124* (33), 17907-17915.

View Article Online
DOI: 10.1039/D6TA02778D

The data that support the findings of this study are openly available in the following Figshare data repository at https://doi.org/10.6084/m9.figshare.32714346.